Supplemental information for:

Secondary organic aerosol formation from ambient air in an oxidation flow reactor in central Amazonia

Brett B. Palm[1,2], Suzane S. de Sá[3], Douglas A. Day[1,2], Pedro Campuzano-Jost[1,2], Weiwei Hu[1,2], Roger Seco[4], Steven J. Sjostedt[5], Jeong-Hoo Park[6,&], Alex B. Guenther[4,7], Saewung Kim[4], Joel Brito[8,@], Florian Wurm[8], Paulo Artaxo[8], Ryan Thalman[9,^], Jian Wang[9], Lindsay D. Yee[10], Rebecca Wernis[11], Gabriel Isaacman-VanWertz[10,#], Allen H. Goldstein[10,11], Yingjun Liu[3,*], Stephen R. Springston[9], Rodrigo Souza[12], Matt K. Newburn[13], M. Lizabeth Alexander[13], Scot T. Martin[3,14], Jose L. Jimenez[1,2]

[1]Cooperative Institute for Research in Environmental Sciences, University of Colorado, Boulder, USA
[2]Dept. of Chemistry, University of Colorado, Boulder, USA
[3]School of Engineering and Applied Sciences, Harvard University, Cambridge, MA, USA
[4]Dept. of Earth System Science, University of California, Irvine, USA
[5]Earth System Research Laboratory, National Oceanic and Atmospheric Administration, Boulder, CO, USA
[6]National Center for Atmospheric Research, Boulder, CO, USA
[7]Div. of Atmospheric Sciences & Global Change, Pacific Northwest National Laboratory, Richland, WA, USA
[8]Institute of Physics, University of São Paulo, Brazil
[9]Environmental and Climate Sciences Department, Brookhaven National Laboratory, Upton, NY, USA
[10]Department of Environmental Science, Policy, and Management, University of California, Berkeley, CA, USA
[11]Department of Civil and Environmental Engineering, University of California, Berkeley, CA, USA
[12]University of the State of Amazonas, Manaus, Brazil
[13]Environmental and Molecular Sciences Laboratory, Pacific Northwest National Laboratory, Richland, WA, USA
[14]Department of Earth and Planetary Sciences, Harvard University, Cambridge, MA, USA
[&]Now at: Climate and Air Quality Research Department, National Institute of Environmental Research (NIER), Incheon, 22689, Republic of Korea
[@]Now at: Laboratory for Meteorological Physics (LaMP), Université Clermont Auvergne, F-63000 Clermont-Ferrand, France.
[^]Now at Department of Chemistry, Snow College, Richfield, UT, USA
[#]Now at Department of Civil and Environmental Engineering, Virginia Tech, USA
[*]Now at Department of Environmental Science, Policy, and Management, University of California, Berkeley, USA

S1   Electrical charge state of particles produced in the OFR

In laboratory measurements after the campaign, the electrical charge state of particles produced in the OFR was investigated, to rule out important effects of charging in the size distribution dynamics. Ambient laboratory air was sampled into the OFR through a high efficiency particulate air (HEPA) filter that had been used in many previous studies to remove particles from air. The output of this filter contained many organic vapors that off-gassed from the filter. Particles nucleated and grew rapidly in the OFR by subjecting this air to OH oxidation, and the particle size distribution was sampled using a TSI 3936 Scanning Mobility Particle Sizer (SMPS). The full particle size distribution was first measured by sampling particles through a TSI 3077 Kr-85 neutralizer to achieve equilibrium charge distribution. Next, the size distribution was sampled without passing through a neutralizer, measuring just the relative fraction of particles that became charged in the OFR. The results, illustrated in Fig. S3, show that approximately an order of magnitude fewer particles were charged in the OFR without the neutralizer than with it. This amount was consistent with the charging expected from natural processes (e.g., cosmic rays) and suggest that chemistry in the OFR (e.g., photoelectric particle charging from the UV lamps) does not lead to substantial particle charging.

References:

DeCarlo, P. F., Slowik, J. G., Worsnop, D. R., Davidovits, P. and Jimenez, J. L.: Particle Morphology and Density Characterization by Combined Mobility and Aerodynamic Diameter Measurements. Part 1: Theory, Aerosol Sci. Technol., 38, 1185–1205, doi:10.1080/027868290903907, 2004.

Kuwata, M., Zorn, S. R. and Martin, S. T.: Using elemental ratios to predict the density of organic material composed of carbon, hydrogen, and oxygen., Environ. Sci. Technol., 46, 787–94, doi:10.1021/es202525q, 2012.

Lambe, A. T., Ahern, A. T., Williams, L. R., Slowik, J. G., Wong, J. P. S., Abbatt, J. P. D., Brune, W. H., Ng, N. L., Wright, J. P., Croasdale, D. R., Worsnop, D. R., Davidovits, P. and Onasch, T. B.: Characterization of aerosol photooxidation flow reactors: heterogeneous oxidation, secondary organic aerosol formation and cloud condensation nuclei activity measurements, Atmos. Meas. Tech., 4, 445–461, doi:10.5194/amt-4-445-2011, 2011.

Li, R., Palm, B. B., Ortega, A. M., Hlywiak, J., Hu, W., Peng, Z., Day, D. A., Knote, C., Brune, W. H., de Gouw, J. A. and Jimenez, J. L.: Modeling the Radical Chemistry in an Oxidation Flow Reactor: Radical Formation and Recycling, Sensitivities, and the OH Exposure Estimation Equation, J. Phys. Chem. A, 119, 4418–4432, doi:10.1021/jp509534k, 2015.

Lide, D. R.: CRC Handbook of Chemistry and Physics, 94th Edition, 2013-2014, 2013.

McMurry, P. H. and Grosjean, D.: Gas and aerosol wall losses in Teflon film smog chambers, Environ. Sci. Technol., 19, 1176–82, doi:10.1021/es00142a006, 1985.

McMurry, P. H. and Rader, D. J.: Aerosol Wall Losses in Electrically Charged Chambers, Aerosol Sci. Technol., 4, 249–268, doi:10.1080/02786828508959054, 1985.

Middlebrook, A. M., Bahreini, R., Jimenez, J. L. and Canagaratna, M. R.: Evaluation of Composition-Dependent Collection Efficiencies for the Aerodyne Aerosol Mass Spectrometer using Field Data, Aerosol Sci. Technol., 46, 258–271, doi:10.1080/02786826.2011.620041, 2012.

Palm, B. B., Campuzano-Jost, P., Ortega, A. M., Day, D. A., Kaser, L., Jud, W., Karl, T., Hansel, A., Hunter, J. F., Cross, E. S., Kroll, J. H., Peng, Z., Brune, W. H. and Jimenez, J. L.: In situ secondary organic aerosol formation from ambient pine forest air using an oxidation flow reactor, Atmos. Chem. Phys., 16, 2943–2970, doi:10.5194/acp-16-2943-2016, 2016.

Peng, Z., Day, D. A., Stark, H., Li, R., Lee-Taylor, J., Palm, B. B., Brune, W. H. and Jimenez, J. L.: HO_x radical chemistry in oxidation flow reactors with low-pressure mercury lamps systematically examined by modeling, Atmos. Meas. Tech., 8, 4863–4890, doi:10.5194/amt-8-4863-2015, 2015.

Salcedo, D., Onasch, T. B., Dzepina, K., Canagaratna, M. R., Zhang, Q., Huffman, J. A., DeCarlo, P. F., Jayne, J. T., Mortimer, P., Worsnop, D. R., Kolb, C. E., Johnson, K. S., Zuberi, B., Marr, L. C., Volkamer, R., Molina, L. T., Molina, M. J., Cardenas, B., Bernabé, R. M., Márquez, C., Gaffney, J. S., Marley, N. A., Laskin, A., Shutthanandan, V., Xie, Y., Brune, W., Lesher, R., Shirley, T. and Jimenez, J. L.: Characterization of ambient aerosols in Mexico City during the MCMA-2003 campaign with Aerosol Mass Spectrometry: results from the CENICA Supersite, Atmos. Chem. Phys., 6, 925–946, doi:10.5194/acp-6-925-2006, 2006.

Williams, J., Keßel, S. U., Nölscher, A. C., Yang, Y., Lee, Y., Yáñez-Serrano, A. M., Wolff, S., Kesselmeier, J., Klüpfel, T., Lelieveld, J. and Shao, M.: Opposite OH reactivity and ozone cycles in the Amazon rainforest and megacity Beijing: Subversion of biospheric oxidant control by anthropogenic emissions, Atmos. Environ., 125, 112–118, doi:10.1016/j.atmosenv.2015.11.007, 2016.

Tables:

Table S1. SOA yields and corresponding OA concentrations for various compounds, measured by standard addition followed by OH or O_3 oxidation in an OFR during GoAmazon2014/5.

Compound + oxidant	SOA yield	OA concentration ($\mu g\ m^{-3}$)
β-caryophyllene + OH	0.52	15
β-caryophyllene + O_3	0.27	25
Longifolene + OH	0.51	25
Sesquiterpenes (average)	0.43	22
Limonene + OH	0.30	20
Limonene + O_3	0.17	11
β-pinene + OH	0.18	28
α-pinene + OH	0.11	20
α-pinene + O_3	0.21	15
Monoterpenes (average)	0.20	19
Toluene	0.11	10
Isoprene	0.06	23

Fig. S1. Pictures of the OFRs operated at the T3 site.
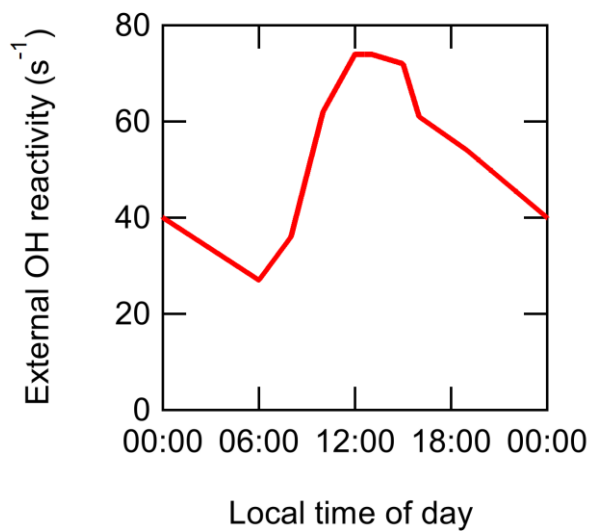
Fig. S2. Mean ambient OH reactivity used as a parameter in the equation to estimate OH exposure in the OFR, shown as a function of local time of day. This diurnal cycle of OH reactivity was adapted and smoothed from Williams et al. (2016).
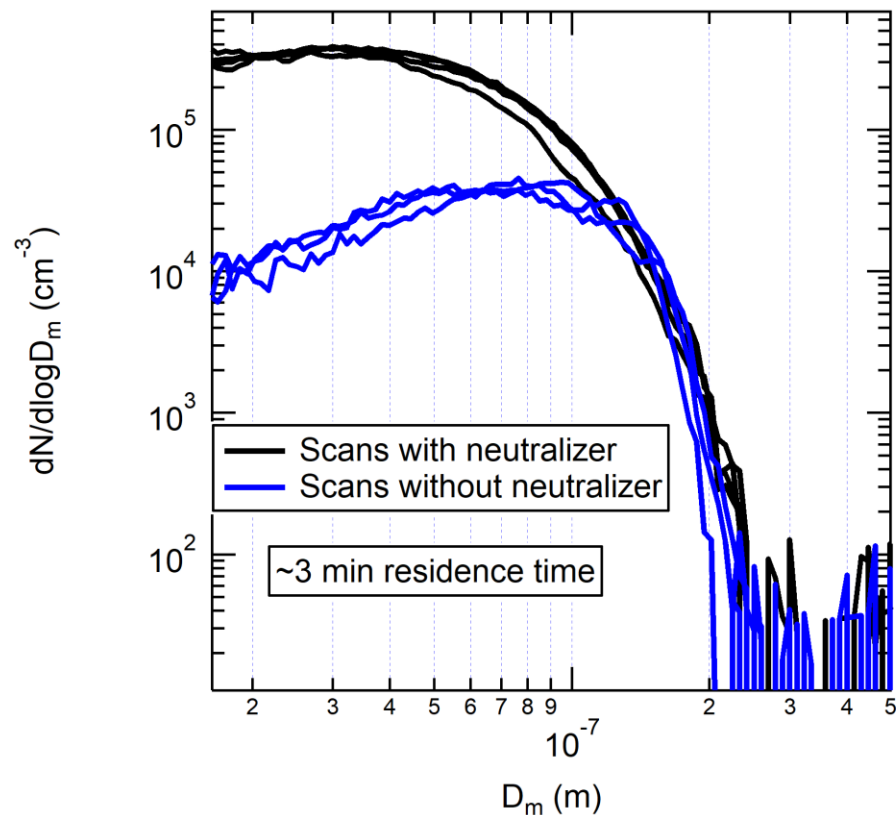
Fig. S3. Particle number size distributions measured with and without first passing through a charge neutralizer. The particles were produced via OH oxidation in an OFR. Air was sampled through a "dirty" particle filter, which off-gassed SOA-precursor gases into the OFR. Without the neutralizer, an order of magnitude fewer particles were charged in the OFR. This is consistent with natural charging processes (e.g., cosmic rays) and suggests the OFR does not inherently produce charged particles.
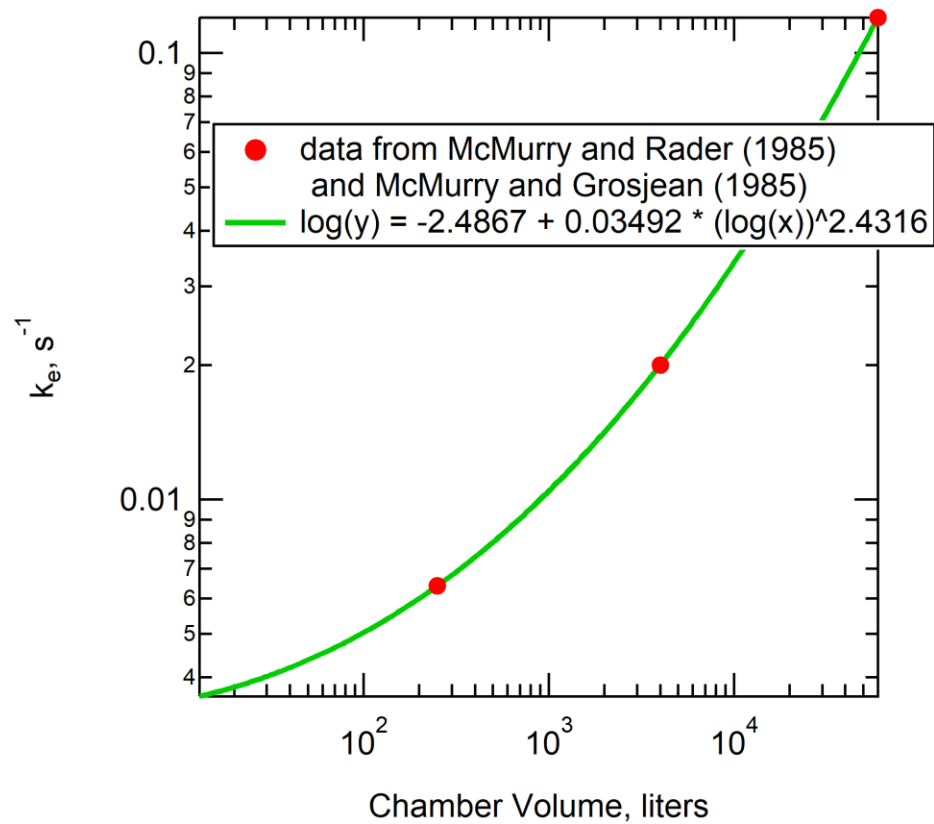
Fig. S4. Coefficient of eddy diffusion (k_e) as a function of chamber volume, as first used for the LVOC fate correction in Palm et al. (2016). The parameterization is based on measurements presented in McMurry and Rader (1985) and McMurry and Grosjean (1985).
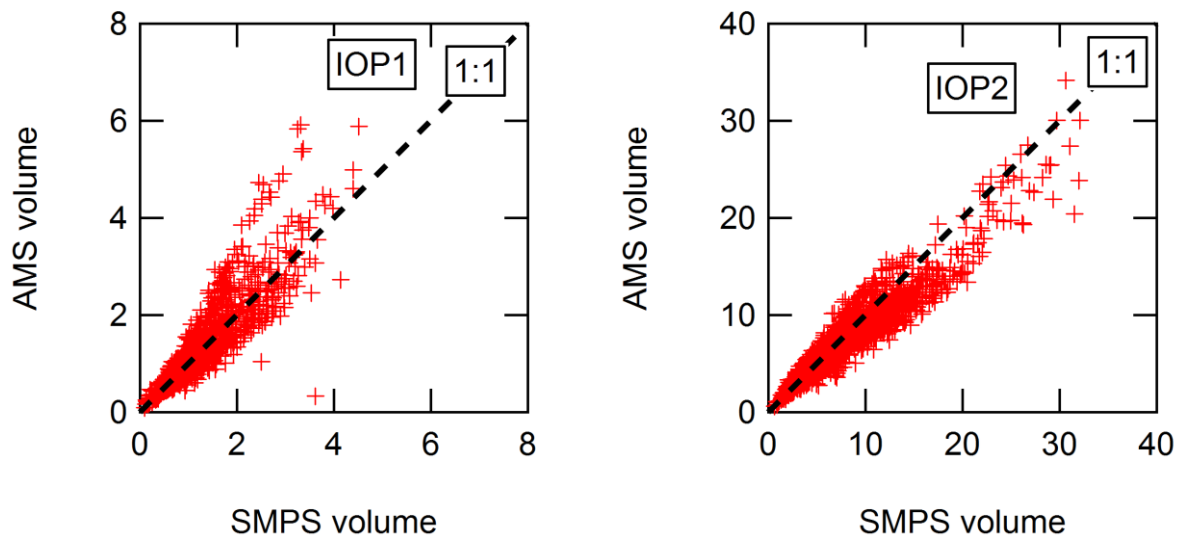
Fig. S5. Aerosol volume measured in the AMS vs. in the SMPS for IOP1 and IOP2. The AMS mass was converted to volume using species densities of 1.75 g cm^{-3} for SO4, NO3, and NH4, 1.52 g cm^{-3} for Chl (DeCarlo et al., 2004; Salcedo et al., 2006; Lide, 2013), and the parameterization for OA density using elemental ratios described in Kuwata et al. (2012). AMS data was calculated using CE=1 during IOP1 and a composition-dependent CE (mostly CE=0.5; Middlebrook et al., 2012) during IOP2.
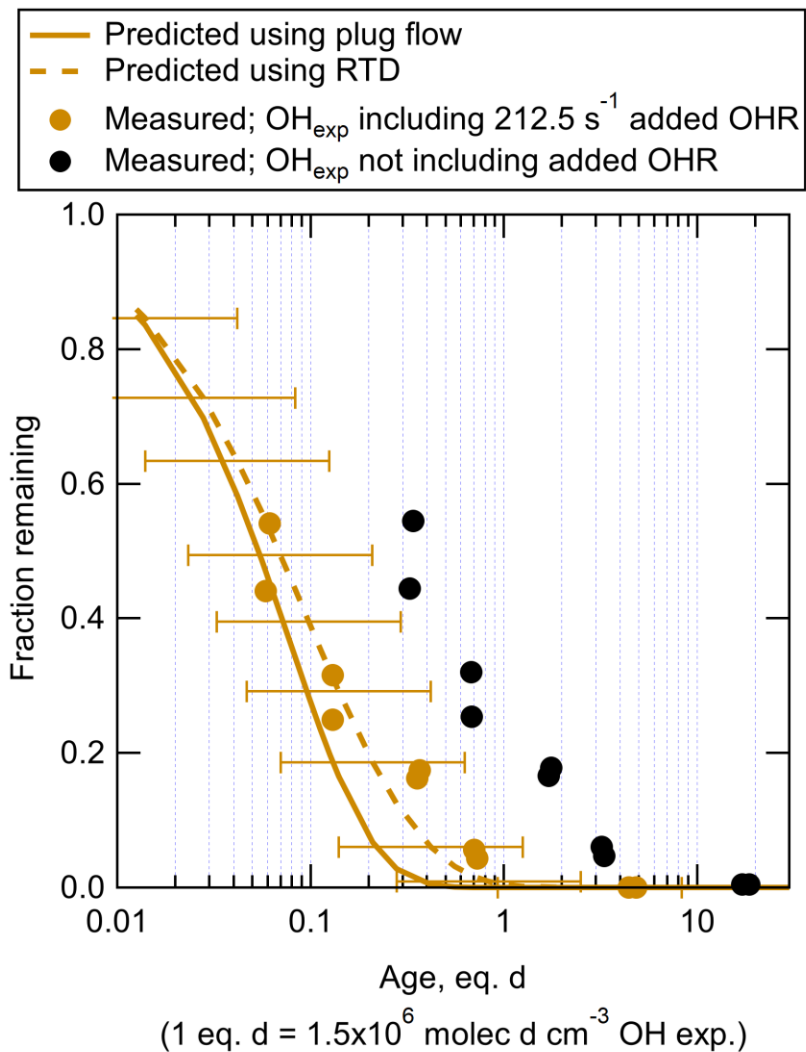
Fig. S6. Fraction of injected isoprene remaining after OH oxidation in the OFR, as a function of photochemical age calculated with and without including the added 215 s^{-1} OHR from the 85 ppb injected isoprene. Binned averages of the fraction remaining are also shown, compared to the amount predicted to remain assuming either plug flow or using the RTD of particles from Lambe et al. (2011). Factor-of-3 error bars are shown for the prediction using RTD, representing the uncertainty in the model-derived OH$_{exp}$ estimation equation (Li et al., 2015; Peng et al., 2015). OH suppression due to high OHR is illustrated by the fact that predicted isoprene decay falls outside the error bars of the predicted decay, unless the added OHR is included in the OH$_{exp}$ calculation.
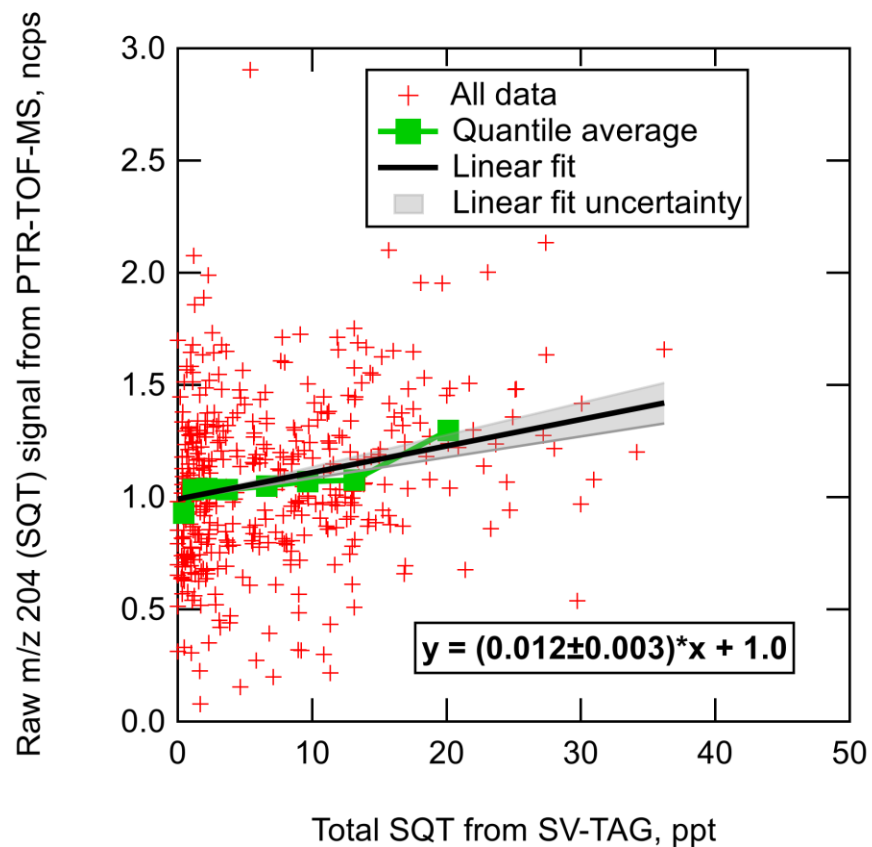
Fig. S7. Scatterplot of raw signal of SQT at *m/z* 204 in the PTR-TOF-MS (while sampling with NO⁺ reagent ion, not background corrected) versus total SQT signal measured by the SV-TAG in ambient air during the dry season. Quantile bin averages and a linear fit (with uncertainty of slope fit) are also shown.
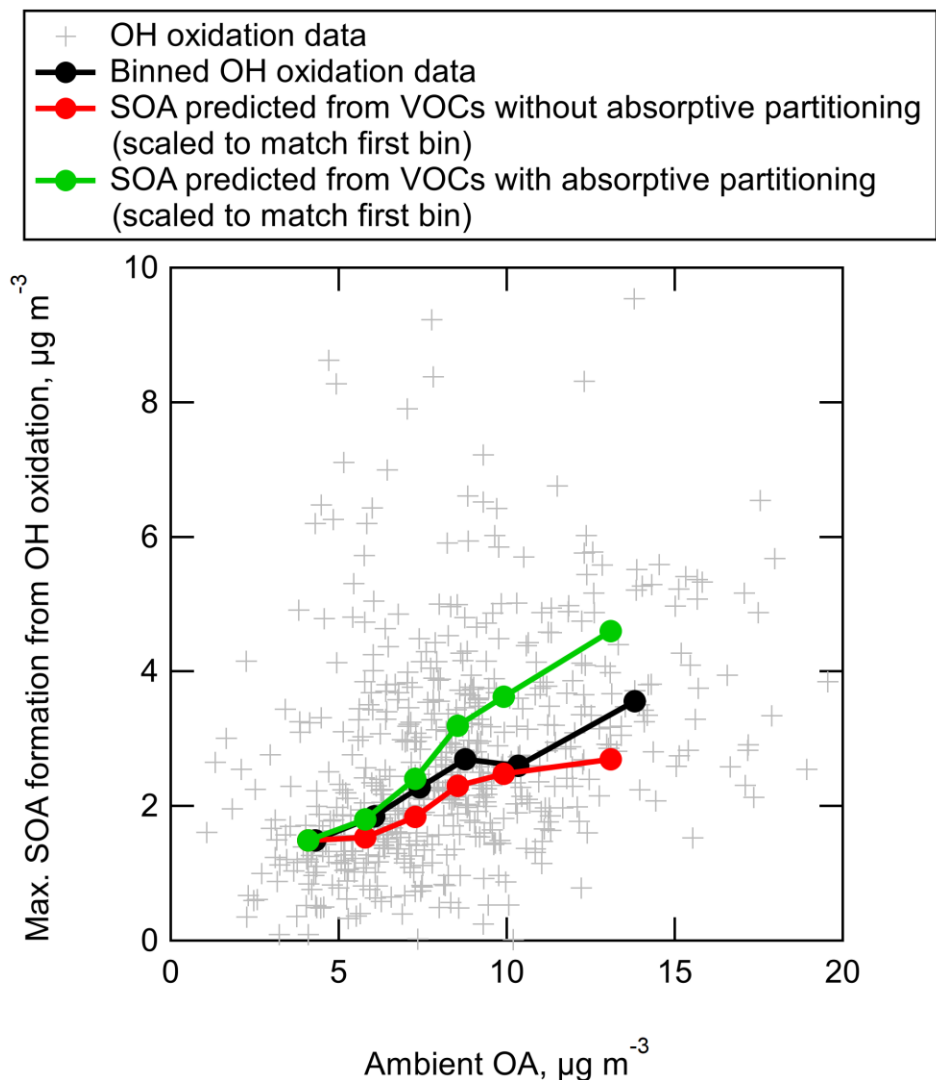
Fig. S8. Maximum SOA formation from OH oxidation during the dry season versus ambient OA concentrations. A binned average of the maximum SOA formation is also shown. For comparison with these measurements, the amount of SOA formation predicted from measured VOCs (as described in Sect. 2.5 and 3.5) was calculated using either constant SOA yields across all OA concentrations (i.e., without absorptive partitioning) or using the OA-concentration dependent SOA yields described in Sect. 2.5 (i.e., with absorptive partitioning). The amounts predicted from VOCs were scaled up so that the first bin of each was equal to the measurements, allowing the slopes to be compared. Since the measurements lie between the two prection extremes, this suggests that the dependence of absorptive partitioning on ambient OA concentratiuons was not as large as calculated from the chamber-based parameterizations discussed in Sect. 2.5.
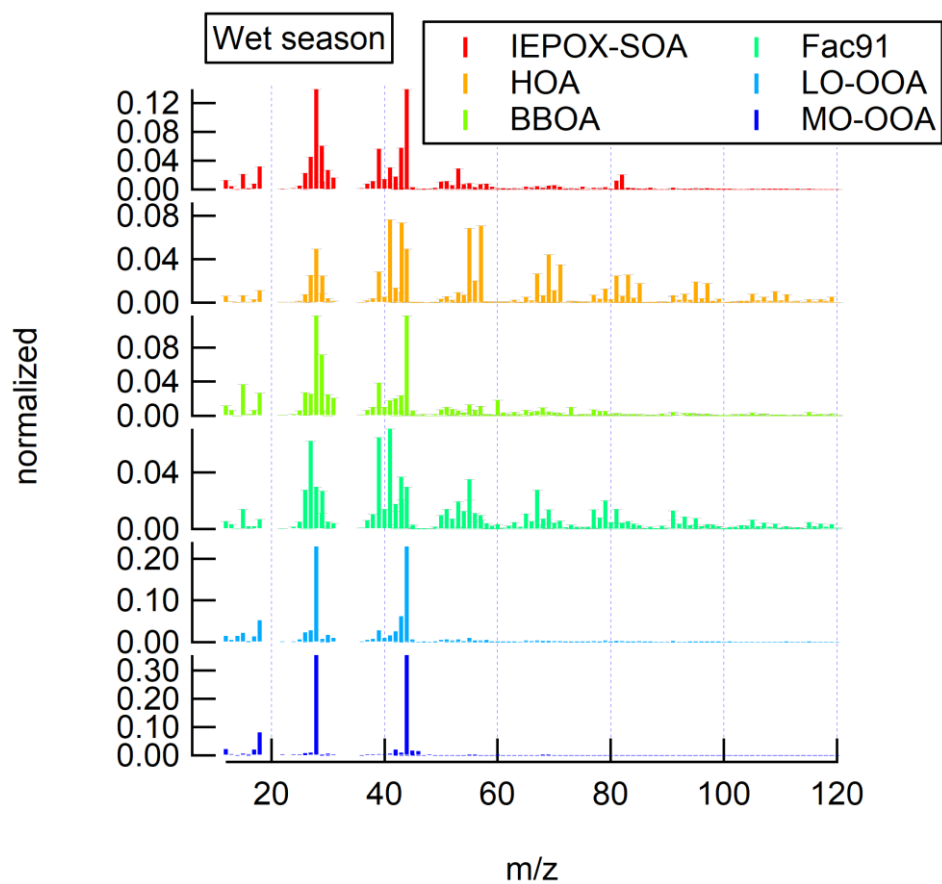
Fig. S9. High-resolution factor profiles for the PMF analysis of the wet season, normalized to a total sum of 1.
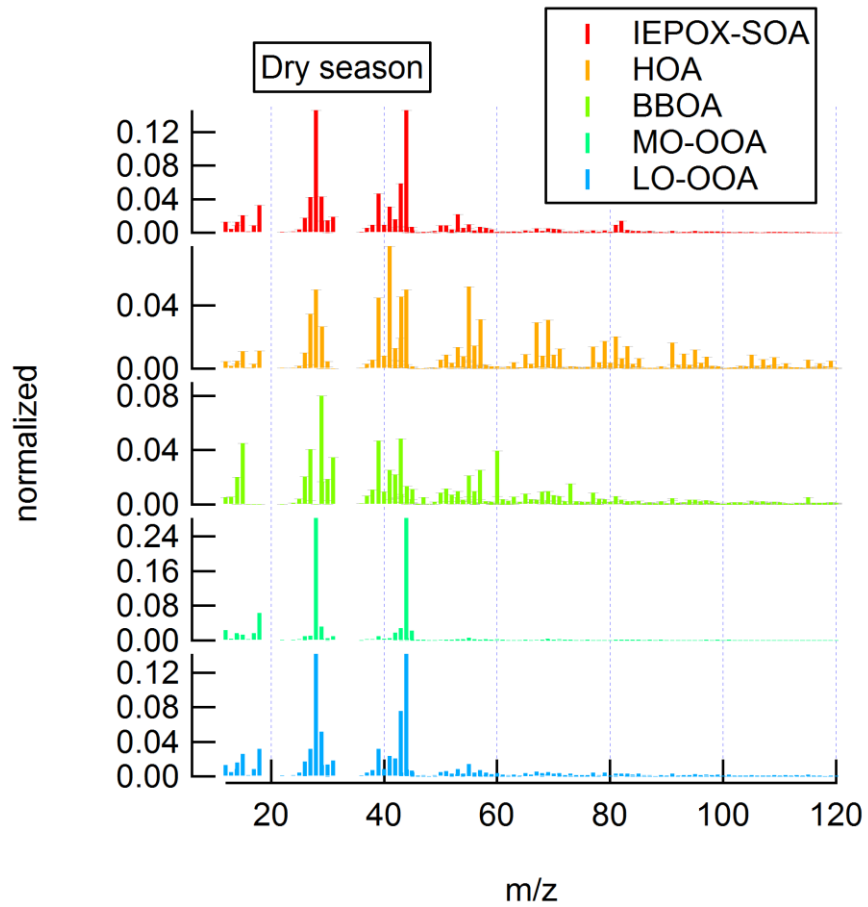
Fig. S10. High-resolution factor profiles for the PMF analysis of the dry season, normalized to a total sum of 1.
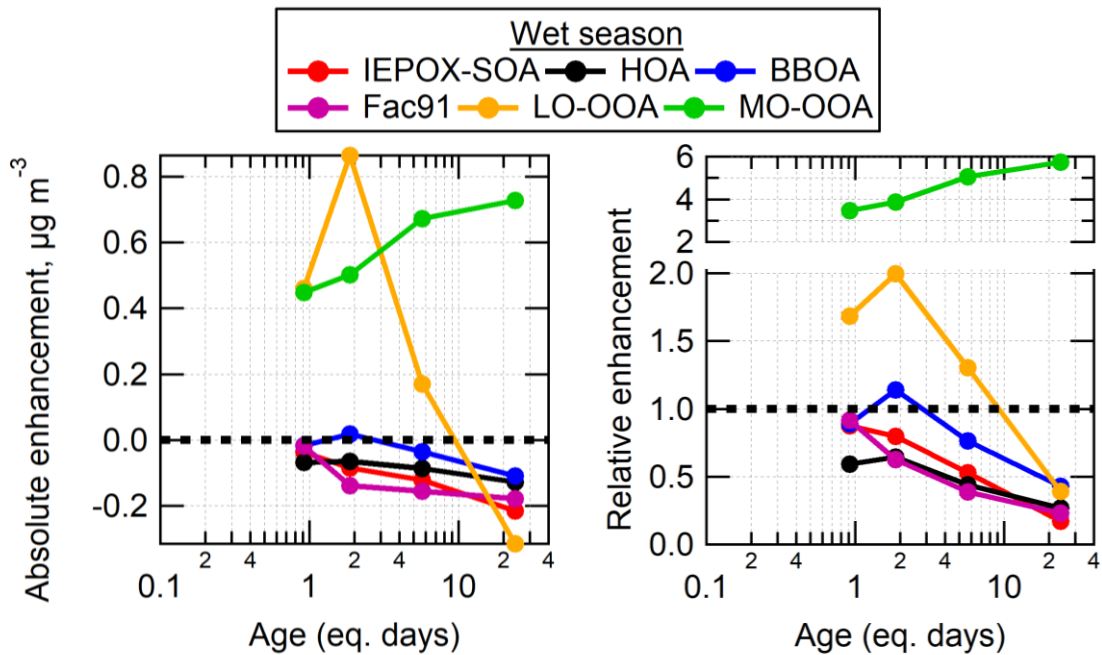
Fig. S11. Absolute (a) and relative (b) changes in PMF factors as a function of eq. days of OH aging in the OH-OFR for the wet season. Note that the y axis in panel (b) is split in order to more clearly show the region below a value of 1.
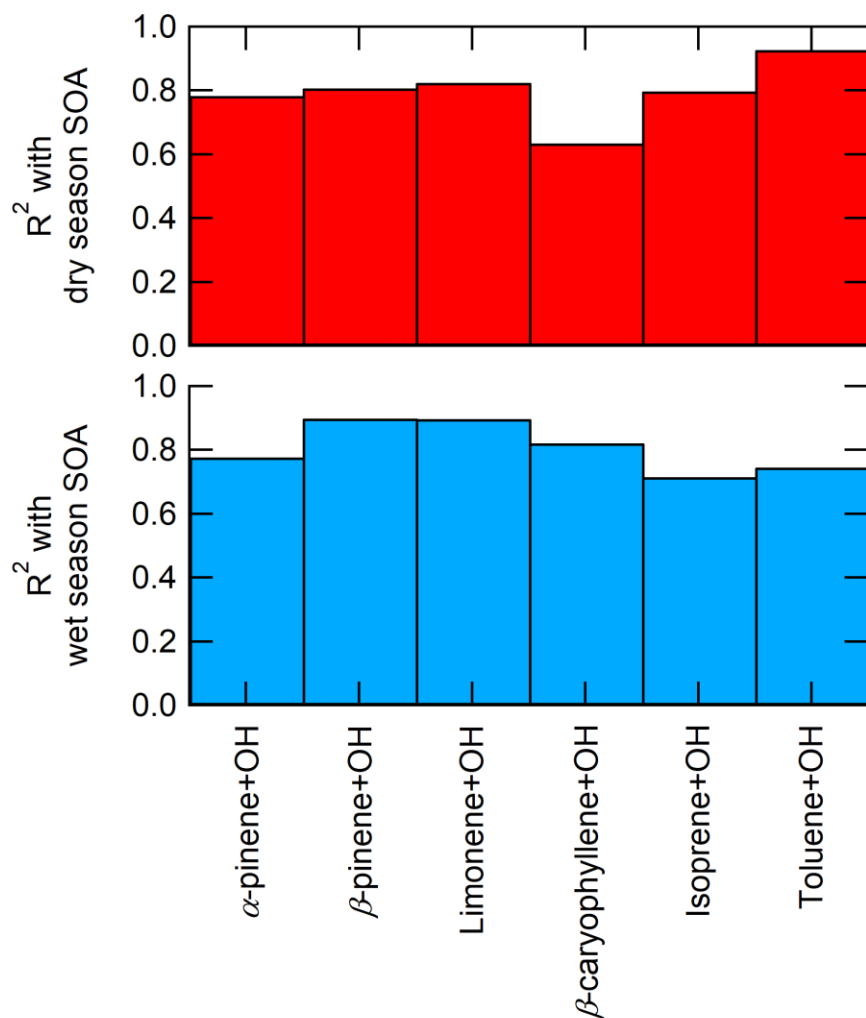
Fig. S12. Correlation coefficients between the SOA formed from OH oxidation of ambient air during the wet and dry with the SOA formed when injecting individual VOCs into the OFR. All spectra were calculated as the difference between the average spectrum of OA after OH oxidation in the OFR minus the average spectrum of concurrent ambient OA. For the spectrum of SOA formed form OH oxidation of ambient air, only data in the range of maximum SOA formation with >1 µg m^{-3} SOA formation were used.
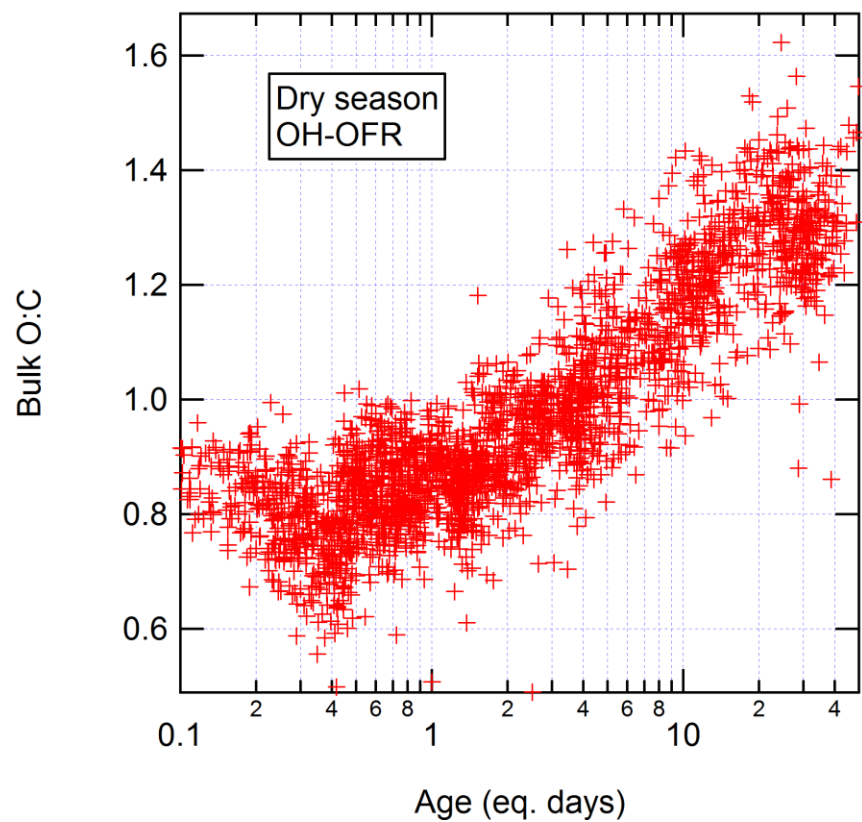
Fig. S13. Elemental O:C ratio of the bulk OA measured after OH oxidation in the OFR, as a function of eq. age of OH aging during the dry season.
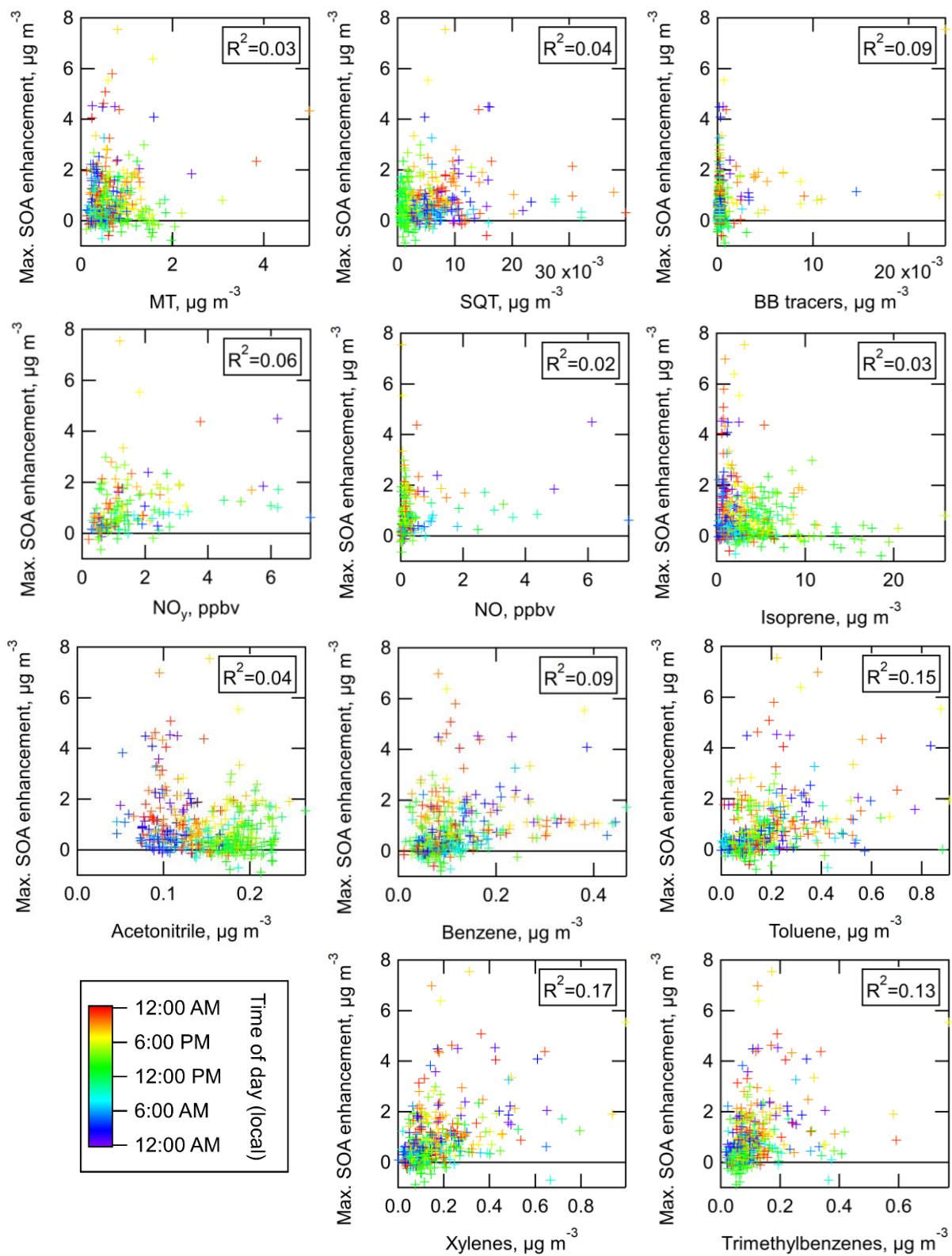
Fig. S14. Scatterplots of maximum measured SOA enhancement from OH oxidation at the T3 site during the wet season, vs. several ambient SOA precursor tracer gases. Correlation coefficients (R^2) are shown for each scatterplot.
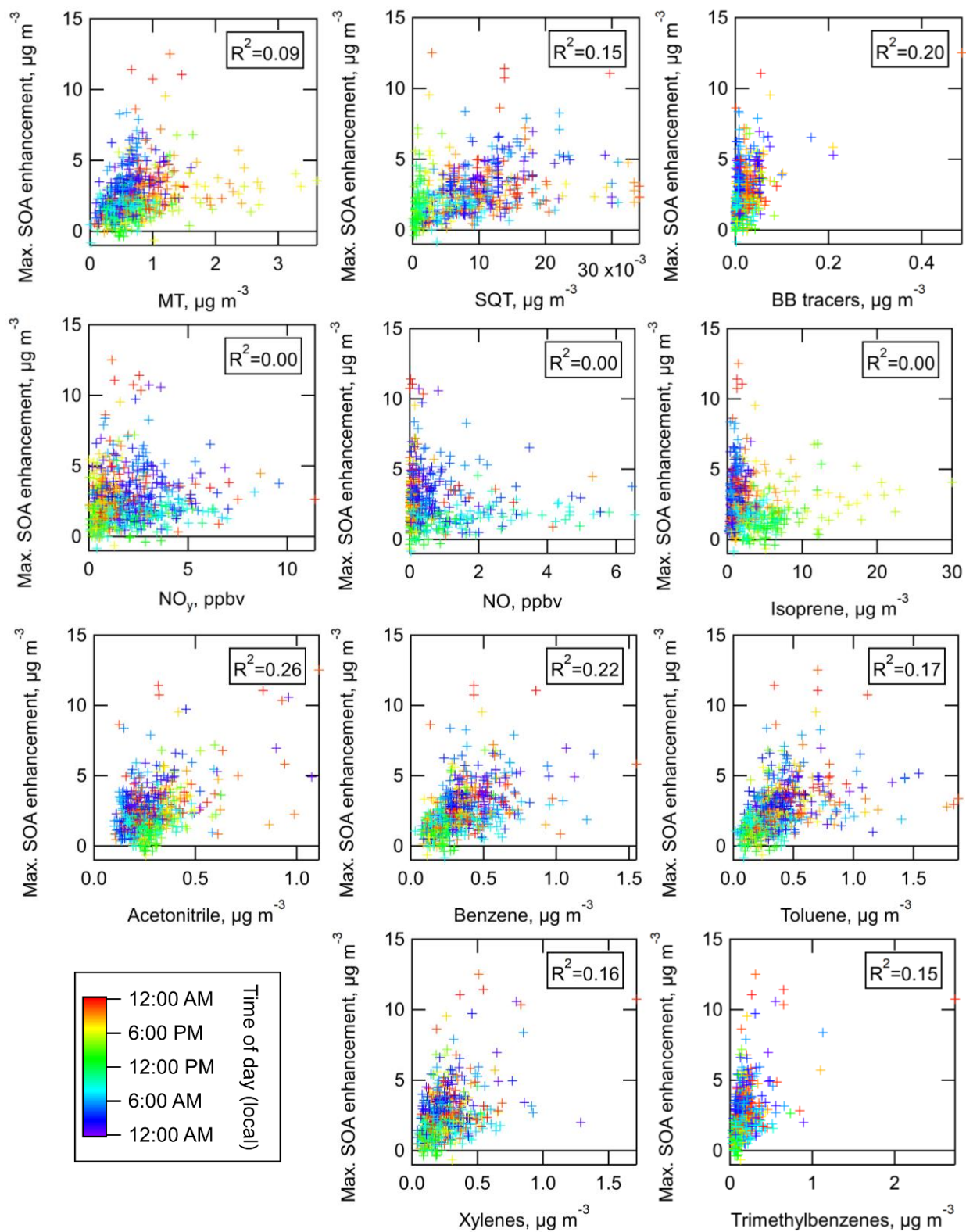
Fig. S15. Scatterplots of maximum measured SOA enhancement from OH oxidation at the T3 site during the dry season, vs. several ambient SOA precursor tracer gases. Correlation coefficients (R^2) are shown for each scatterplot.
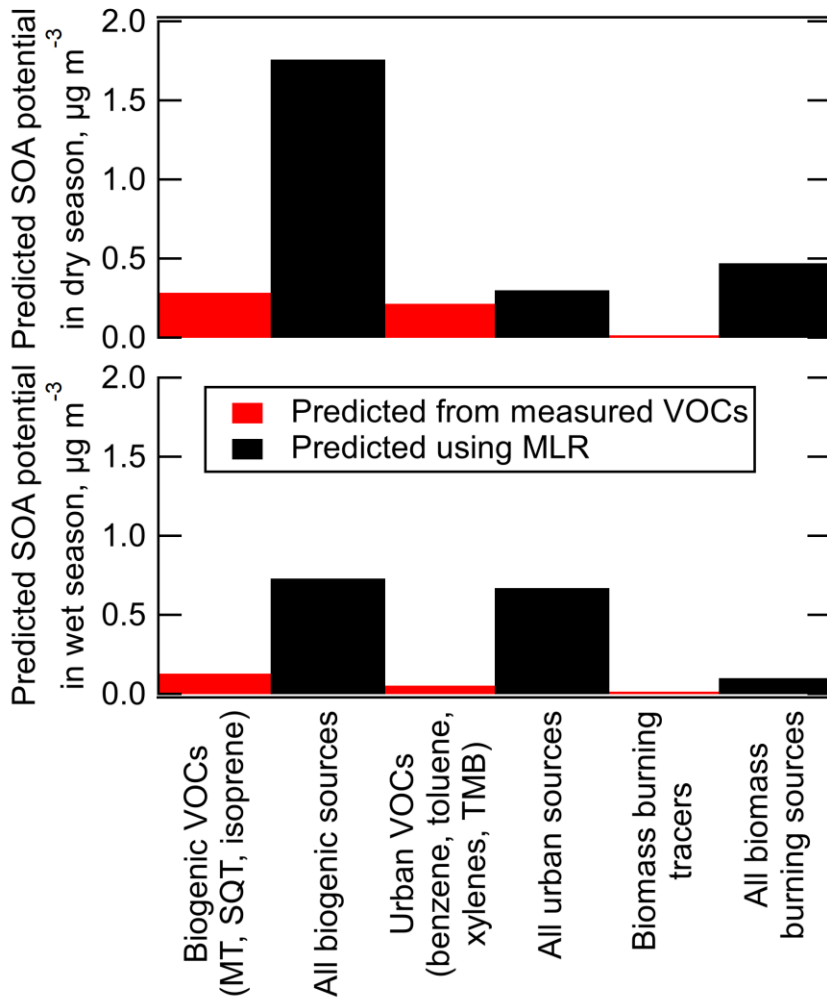
Fig. S16. A comparison between the amount of SOA formation potential predicted from measured VOCs and the amount predicted from each total source from the multi-linear regression analysis in Sect. 3.8, for both wet and dry seasons.